Two-component thermosensitive hydrogels: Phase separation affecting rheological behavior

Anna Abbadessa[a], Mariana Landín[b], Erik Oude Blenke[a], Wim E. Hennink[a], Tina Vermonden[a,*]

[a] Department of Pharmaceutics, Utrecht Institute for Pharmaceutical Sciences (UIPS), Science for Life, Faculty of Science, Utrecht University, P.O. Box 80082, 3508 TB Utrecht, The Netherlands
[b] Department of Pharmacology, Pharmacy and Pharmaceutical Technology, University of Santiago, P.O. Box 15782, Santiago de Compostela, Spain

ARTICLE INFO

ABSTRACT

Extracellular matrices are mainly composed of a mixture of different biopolymers and therefore the use of two or more building blocks for the development of tissue-mimicking hydrogels is nowadays an attractive strategy in tissue-engineering. Multi-component hydrogel systems may undergo phase separation, which in turn can lead to new, unexpected material properties. The aim of this study was to understand the role of phase separation on the mechanical properties and 3D printability of hydrogels composed of triblock copolymers of polyethylene glycol (PEG) and methacrylated poly(N-(2-hydroxypropyl) methacrylamide-mono/dilactate) (pHPMAlac) blended with methacrylated hyaluronic acid (HAMA). To this end, hydrogels composed of different concentrations of PEG/pHPMAlac and HAMA, were analyzed for phase behavior and rheological properties. Subsequently, phase separation and rheological behavior as function of the two polymer concentrations were mathematically processed to generate a predictive model. Results showed that PEG/pHPMAlac/HAMA hydrogels were characterized by hydrophilic, HAMA-richer internal domains dispersed in a more hydrophobic continuous phase, composed of PEG/pHPMAlac, and that the volume fraction of the dispersed phase increased by increasing HAMA concentration. Storage modulus, yield stress and viscosity increased with increasing HAMA concentration for low/medium HAMA contents ($\leq 0.75\%$ w/w), while a further increase of HAMA resulted in a decrease of the mentioned properties. On the other hand, by increasing the concentration of PEG/pHPMAlac these rheological properties were enhanced. The generated models showed a good fitting with experimental data, and were used to identify an exemplary 3D printability window for PEG/pHPMAlac/HAMA hydrogels, which was verified by rheological characterization and preparation of 3D printed scaffolds. In conclusion, a clear relationship between phase separation and rheological behavior in these two-component hydrogels can be described by complex functions of the two polymer concentrations. The predictive model generated in this study can be used as a valid tool for the identification of hydrogel compositions with desired, selected characteristics.

1. Introduction

Hydrogels are networks of hydrophilic natural and/or synthetic polymers, able to absorb and retain large amounts of water. Because of their capacity to entrap cells and biologically active molecules, *e.g.* therapeutic proteins, they are currently under investigation for tissue engineering (TE) [1,2] and drug delivery applications [3–8]. Especially for regenerative medicine purposes, hydrogels are of interest because they can mimic the aqueous nature and mechanical properties of soft tissues and warrant a cell-friendly environment [9]. Moreover, biodegradable hydrogels offer a temporary support, which can be progressively replaced by new tissue components, synthesized by embedded or recruited cells [10–12]. In addition, hydrogels having specific rheological properties can be processed into desired shapes by injection molding or more sophisticated three-dimensional (3D) printing-based manufacturing procedures [13–19]. This aspect is especially important to generate patient-customized implants, which eventually may facilitate clinical translation of TE constructs.
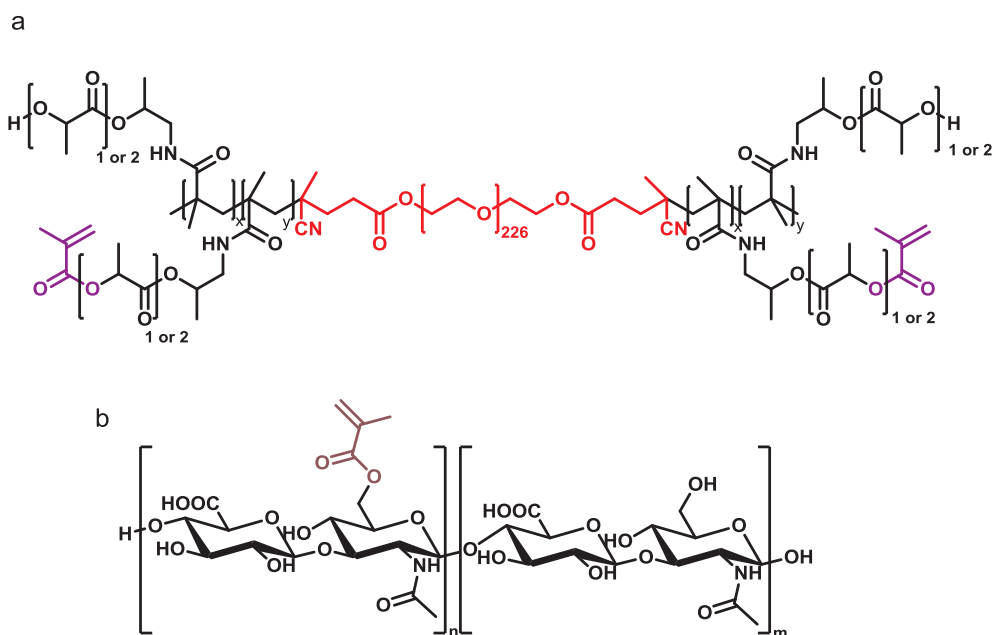
Hydrogels based on triblock copolymers of polyethylene glycol (PEG) and methacrylated poly(N-(2-hydroxypropyl) methacrylamide-mono/dilactate) (pHPMAlac) have gained interest during the last decade for their tunable thermosensitive behavior, mechanical and degradation profiles as well as 3D printability and cytocompatibility [20–22]. Our more recent studies have shown that by blending these PEG/methacrylated pHPMAlac triblock copolymers with UV cross-linkable polysaccharides, *i.e.* methacrylated chondroitin sulfate [23] or methacrylated hyaluronic acid [24], hydrogels with improved mechanical characteristics and degradation profiles can be obtained. Specifically, the more pronounced thermosensitivity, shear thinning and yield stress behavior led to a superior 3D printability of hydrogels based on polysaccharides and PEG/methacrylated pHPMAlac copolymers compared with hydrogels only composed of PEG/methacrylated pHPMAlac copolymers [23,24]. Nevertheless, mechanistic insights behind the beneficial effect on mechanical properties due to the addition of polysaccharides to hydrogels of PEG/methacrylated pHPMAlac are lacking. Visual inspection of these hydrogels pointed to the possibility of aqueous two phase separation (ATPS) [23], similar to that described for some pairs of water soluble polymers, such as the combination of PEG and dextran [25]. The miscibility of two polymers in water is governed by the following equation:

$$\Delta G_{mix} = \Delta H_{mix} - T\Delta S_{mix} \tag{1}$$

where ΔG_{mix} is the free energy of mixing, ΔH_{mix} is the enthalpy of mixing, T is the absolute temperature and ΔS_{mix} is the entropy of mixing. Phase separation occurs when ΔG_{mix} is positive, and this is possible when $\Delta H_{mix} > 0$ and $> T\Delta S_{mix}$. For polymeric mixtures in water, it has been found that ΔS_{mix} is usually very low, and thus even small positive values of ΔH_{mix} result in positive ΔG_{mix} values [25]. ATPS has found valuable applications in polymeric microparticles fabrication [26,27] as well as in the extraction and separation of biological molecules and cell subtypes [28–30]. Moreover, ATPS-like phenomena have been observed in hydrogels investigated for biomedical applications, and a positive effect on the morphology of embedded cells as well as on the new tissue formation has been reported [31].

Interestingly, for telechelic ABA-like amphiphilic triblock copolymers, *e.g.* PEG end-capped with aliphatic blocks [32] and PEG flanked by pHPMAlac outer blocks [21,33], aqueous phase separation has been described in simple binary systems (one type of polymer in water), at certain conditions of polymer concentration and temperature. In this case, phase separation is attributed to the formation of polymer-rich regions composed of highly "packed" and interconnected polymeric clusters (flower-like micelles), and water-rich regions mainly composed of free micelles and hydrated single polymeric chains [34]. Similarly, phase separation observed for hydrogels composed of highly methacrylated hyperbranched polyglycerol, was explained by the co-existence of polymer-rich regions based on partially dehydrated hydrophobic blocks and water-rich regions containing highly hydrated hydrophilic polymeric portions [35].

Our hypothesis is that ATPS in hydrogels composed of polysaccharides and PEG/methacrylated pHPMAlac copolymers plays an essential role on the thermosensitivity as well as on fluid-flow properties, *e.g.* shear thinning and yield stress of these hydrogels, and consequently on hydrogel 3D printability. To assess this aspect and to provide a full understanding of the inner micro-organization of these hydrogels, polymeric mixtures of methacrylated hyaluronic acid and PEG/methacrylated pHPMAlac copolymer were prepared and analyzed for their hydrophilic/hydrophobic balance, and possible preferential distribution of the two polymers within the hydrogel. Moreover, rheological properties as function of the two polymers' concentration (and phase separation extent) were studied. Finally, to mathematically study the dependency of phase separation extent and rheological properties from the two polymeric contents, and to create a predictive model, experimental data were integrated using Artificial Neural Networks (ANNs). ANNs have been firstly applied in the pharmaceutical field to overcome the shortcomings of the traditional multiple regression analysis [36]. Due to the complexity of the interpretation of ANNs models, they are often combined with other Artificial Intelligence technologies such as fuzzy logic, giving hybrid systems [37,38]. The neurofuzzy logic technology used in this study combines the adaptive learning capabilities from ANNs and the ability to generalize rules of fuzzy. It allows the definition of the design space with a relative small amount of data and the generation of complex non-linear models of easy and quick numerical solutions. Additionally, fuzzy logic technology enables generation of linguistic rules in order to explain the dependency of the *outputs* from the *input* parameters [39]. In this study, concentrations of PEG/methacrylated pHPMAlac copolymer and methacrylated hyaluronic acid were used as *input* parameters, and phase separation extent and rheological properties were used as *outputs*.

a

b

Scheme 1. Chemical structure of polymers used in this study. Structure of $M_{10}P_{10}$, composed of a PEG-based mid-block (in red) flanked by two pHPMA-lac outer blocks (in black) being partially methacrylated (in purple, a). Chemical structure of HAMA (b). (For interpretation of the references to colour in this figure legend, the reader is referred to the web version of this article.)

2. Materials and methods

2.1. Materials

All chemicals and solvents were obtained from Sigma-Aldrich (Zwijndrecht, the Netherlands) and Biosolve (Valkenswaard, the Netherlands), respectively, unless indicated otherwise. Chemicals and solvents were used as received. Hyaluronic acid (HA, 120 kDa) was supplied by Lifecore Biomedical (Chaska, MN, USA). L-lactide was obtained from Corbion Purac (Gorinchem, The Netherlands), phosphate buffered saline pH 7.4 (PBS) from Braun (Melsungen, Germany) and Irgacure 2959 was donated by BASF (Ludwigshafen, Germany). Albumin-fluorescein isothiocyanate conjugate (FITC-BSA) and Nile Red (NR) were purchased from Sigma-Aldrich. Weigert's hematoxylin (solution A + B), formaldehyde and xylene were supplied by Klinipath BV (Duiven, The Netherlands). Fast green FCF was ordered from MP Biomedicals (Eindhoven, The Netherlands), safranin-O from VWR (Amsterdam, The Netherlands), and paraffin from Leica Biosystems (Eindhoven, The Netherlands).

2.2. Synthesis and characterization of polymers

A triblock copolymer composed of a PEG (10 kDa) mid-block flanked by two pHPMAlac (mono/dilactate molar ratio = 75:25) outer blocks (chemical structure reported in Scheme 1a) was synthesized by free radical polymerization, and further partially methacrylated as previously described [20]. The triblock copolymer was characterized by Gel Permeation Chromatography (GPC), Proton Nuclear Magnetic Resonance (^{1}H NMR) and UV–VIS spectrophotometry before and after methacrylation as described previously [20,40]. The triblock copolymer is further abbreviated as M_0P_{10}, whereas its methacrylated derivative as $M_{10}P_{10}$, where M_0 and M_{10} refer to a degree of methacrylation (DM) of 0 and 10% of the lactate side groups, respectively and P_{10} refers to a PEG mid-block of 10 kDa.

HA was methacrylated as previously reported by Hachet et al. with minor adjustments [41]. Briefly, 5 g (12.5 mmol of disaccharide units) of HA was dissolved in 250 ml of ultrapure water and 250 ml of N,N-dimethylformamide (DMF). Next, 5 ml of methacrylic anhydride (33.6 mmol) was added drop-wise at 4 °C, while keeping the pH between 8 and 9 by addition of aqueous NaOH solution (0.5 M). Subsequently, the polymer mixture was stirred overnight at 4 °C, and the polymer was purified by precipitation in cold ethanol and subsequently re-dissolved in water. After two days of dialysis (MWCO = 10–14 kDa) against water at 4 °C, the polymer solution was freeze-dried and the recovered polymer is further referred to as HAMA (chemical structure reported in Scheme 1b). HA and HAMA were characterized by GPC [23]. HAMA was analyzed by ^{1}H NMR (D$_2$O) and the DM defined as the number of methacrylate groups per 100 disaccharide units was calculated according to Eq. (2).

$$DM\ (\%) = \frac{average\ (I_{6.2}, I_{5.8})}{(I_{2.1}-3)/3} \times 100$$

(2)

Table 1
Polymer mixtures based on different concentrations of $M_{10}P_{10}$ and HAMA. The combinations of $M_{10}P_{10}$ and HAMA concentrations marked with a cross (x) were prepared in this study.

$M_{10}P_{10}$	HAMA					
w/w%	0	0.5	0.75	1	1.5	2
0						x[a]
22	x[a,b]	x[a,b]	x[a,b]	x[a,b]	x[a]	x[a,b]
24		x[a]	x[b]			
26		x[a,b]			x[a,b]	
30		x[b]				

[a] Hydrogel compositions tested by confocal microscopy.
[b] Hydrogel compositions tested by rheological analysis.

in which an integration value of 1 is given to the signal at chemical shift of 6.2 ppm. The DM of HAMA was also measured according to a High Performance Liquid Chromatography (HPLC)-based method, as reported previously [24,42].

2.3. Preparation of hydrogels and experimental design

Polymer mixtures containing $M_{10}P_{10}$ and HAMA at different concentrations (Table 1) were prepared by dissolving the two polymers in PBS (pH = 7.4) in the same vial under mild stirring at 4 °C overnight. These polymer mixtures (and the corresponding hydrogels) are further abbreviated as MH (referring to the presence of $\underline{M}_{10}P_{10}$ and $\underline{H}$AMA) followed by the concentration (w/w%) of the two polymers. For instance, MH 22 + 1 is composed of 22% (w/w) of $M_{10}P_{10}$ and 1% (w/w) of HAMA. Contents of $M_{10}P_{10}$ ranging from 22 to 30% (significantly above the critical aggregation concentration [21,43]) and contents of HAMA from 0 to 2% were chosen, based on handling properties and expected thermoresponsivity.

To assess phase separation, hydrogels were analyzed using confocal imaging, safranin-O staining and ^{1}H NMR. Additionally, their rheological properties were determined. Results obtained from confocal imaging and rheological measurements were used to create a predictive model based on neurofuzzy logic technology [39]. The generated model was used to identify an exemplary 3D printability window based on applied constraints, and 3D printed porous constructs were fabricated by an extrusion-based 3D printing procedure.

2.4. Confocal laser scanning microscopy (CLSM)

Freshly prepared MH polymer mixtures were enriched with FITC-BSA (final concentration = 0.2%) and a few grains of NR, and maintained under stirring overnight at 4 °C. FITC-BSA and NR were chosen to stain hydrophilic and hydrophobic domains, respectively [21,33]. Subsequently 100 μl of each polymer mixture was dispensed in duplo in a 96-well plate and incubated at 37 °C for 1 h. Confocal images were obtained using a Yokogawa Cell Voyager 7000S imager (Yokogawa, Tokyo, Japan) at 37 °C. Samples were visualized with a 40× objective employing 488 nm and 561 nm lasers for the excitation of FITC-BSA and NR, respectively. For both fluorophores the used exposure time was 250 ms. Acquisitions were performed using BP525/50 and BP600/37 emission filters for FITC and NR, respectively. Images were recorded for three different locations within each well and for three different Z-stack sections of each location using a Z-stack interval of 3 μm. To quantify the ratio between the domains where NR was dissolved (red areas) and FITC-BSA was predominant (green areas), images were processed using ImageJ 1.45 software. Areas (in pixels) of the red and the green regions were measured for three different acquisition points for each polymer mixture, and a red and a green area were defined as percentage of the total area. From this, a red/green ratio (R/G ratio) was calculated. To investigate the effect of incubation time on phase separation, images were recorded at several time points within the first hour of incubation at 37 °C (*i.e.* 0, 10, 30, 40, 50 and 60 min), and after 2, 3, 8 and 25 h. For early points (< 1 h) pictures were taken using slightly more intense light for the red channel, to compensate for the slow dissolution of NR.

2.5. Safranin-O staining

To assess the localization of HAMA, safranin-O/fast green assay was chosen as a glycosaminoglycan (GAG)-selective staining procedure, which is widely used in tissue engineering for the visualization of GAG-based components in cartilaginous matrices [44–48]. To this end, MH polymer mixtures enriched with 0.05% of Irgacure, were injected into a Teflon mold, incubated at 37 °C for 1 h and UV irradiated for 5 min using a Bluepoint 4 UV lamp (point light source, wavelength range: 300–600 nm, intensity at 5 cm: 80 mW/cm^2, Hönle UV Technology AG, Gräfelfing, Germany) to generate cylindrical UV cross-linked hydrogels. After dehydration using graded series of ethanol/water solutions and a final washing step with xylene, the dehydrated hydrogels were embedded in paraffin and finally sliced into 5 μm thick samples. Safranin-O/fast green assay was performed as previously described in literature [49], and images were collected using an Olympus microscope equipped with a digital camera (Olympus BX51 microscope, Olympus DP70 camera, Hamburg, Germany).

Table 2

Settings used for rheological analysis in oscillation and flow mode.

Procedure	T (°C)	Ramp rate (°C/min)	Shear rate (1/s)	Frequency (Hz)	Strain (%)
Oscillation temperature ramp	4–50	5[a]	–	1	1
Oscillation strain sweep	37	–	–	1	0.01–100
Flow shear rate sweep	37[b]	–	0.006–10000	–	–
Oscillation recovery	37	–	–	1	Step1[c]: 1 step2[c]: 100 step3[c]: 1
Flow recovery	37	–	Step 1[c]: 0.05 step 2[d]: 100 step 3[c]: 0.05	–	–

[a] For a few hydrogel compositions also at 0.75 °C/min.
[b] For a few hydrogel compositions also at T_{gel} and 20 °C.
[c] Duration step = 60 s.
[d] Duration step = 1 s.

2.6. ^{1}H NMR analysis of the two phases

A mixture based on MH 22 + 2 (2.7 ml), prepared as described in 'Preparation of hydrogels and experimental design' was incubated for 1 h at 37 °C and centrifuged at maximal speed (5292g) for 1.5 h at 37 °C. Next, the two phases were collected separately, freeze-dried and further analyzed by ^{1}H NMR (D$_2$O) at room temperature.

2.7. Rheological measurements

Polymer mixtures prepared as described in 'Preparation of hydrogels and experimental design' were analyzed for their rheological properties using a Discovery HR-2 rheometer (TA-Instruments, Etten-Leur, The Netherlands) equipped with a cone-plate measuring geometry (cone diameter: 20 mm, cone angle: 1°, truncation: 27 μm). Samples were analyzed in duplicate using the conditions summarized in Table 2.

The temperature of gelation (T_{gel}) is here referred to as the temperature where the storage modulus (G′) equals the loss modulus (G″) during the temperature ramp experiments, according to a previously reported operational definition [20,22], whereas the shear yield stress is defined as the stress at which G′ crosses G″ during the oscillation strain sweep experiments [50,51]. For a few samples, a recovery test was also performed in oscillation and in flow operating mode at 37 °C to investigate if these gels were capable to fully recover after shear stress.

2.8. Computational modeling

To mathematically study the dependency of phase separation extent and rheological properties from $M_{10}P_{10}$ and HAMA concentrations, and to create a predictive computational model, a database of twelve facts was generated, including MH compositions (Table 1) and corresponding gel properties. Neurofuzzylogic software (FormRules® v4.03, Intelligensys Ltd. UK) was used. The $M_{10}P_{10}$ and HAMA contents (w/w%) were chosen as *input* parameters, whereas R/G ratio, G′ at 37 °C and T_{gel} recorded during oscillation temperature ramps, yield stress recorded during oscillation strain sweeps and viscosity at low shear rate (*i.e.* 0.006 1/s) recorded during flow shear rate sweeps were selected as *output* parameters. The default training parameters of the software were used for modeling. The software contains various statistical fitness criteria. Among them, Structural Risk Minimisation (SRM) was used to model all *outputs* (C_1 = 0.8 and C_2 = 4.8), except T_{gel} that required the use of Leave One Out Cross Validation (LOOCV) to be properly fitted. The significant effect of a single *input* (HAMA or $M_{10}P_{10}$ content) or their interaction on each studied property is pointed out by neurofuzzylogic software by generating sub-models for each *output* parameter. Additionally, through "IF…THEN" rules, every *output* parameter (*e.g.* R/G ratio) is related to the *input* variable (*e.g.* HAMA content) obtaining statements as follows: *"If HAMA content is low, R/G ratio is high and if HAMA content is high, R/G ratio is low"*, where *high* and *low* are always flanked by a membership value (ranging from 0 to 1). The membership value describes how close the predicted value of a property (*e.g.* R/G ratio) is to the highest or lowest experimental value of that property, respectively. To assess the predictability of each generated model, Train Set R-squared values (indicating the percentage of the *output* variability explained by *inputs*) were calculated. Additionally, ANOVA was also carried out to test the statistical significance of each model. Obtaining computed f values higher than critical f values for the degrees of freedom of the model was used as a necessary condition to assert good performance and accuracy of the model. Subsequently, 3D surface charts were created, where *output* parameter values predicted by the models were reported as function of the two *input* parameters. Finally, to provide a practical example of their predictive capacity, the generated models were used for the identification of MH hydrogel compositions with selected properties. Table 3 contains the inclusion criteria that were used to generate a MH composition range with desirable properties for nozzle-based 3D bioprinting applications. 2D charts originating from the top view of the 3D surface charts for each *output* parameter were overlapped and a region of interest, where all inclusion criteria were satisfied was identified.

Table 3
Inclusion criteria for the identification of a MH hydrogel composition range with selected properties.

Property	Desirable range of values	Rationale
Yield stress	≥30 Pa	Shape fidelity after 3D printing extrusion
G′ at 37 °C	≥150 Pa	Shape fidelity after 3D printing extrusion
T_{gel}	≤37 °C	Shape fidelity at physiologically relevant temperatures
Viscosity at low shear	≥500 Pa·s	Shape fidelity after 3D printing extrusion
Total polymer concentration	≤26%	Handling, cell incorporation
R/G ratio	≥75/25	Stability of the mixture in the cartridge

2.9. 3D printing assessment

3D printing of an exemplary MH gel composition with selected properties as predicted by the model was performed using a 3D Discovery bioprinter (RegenHU, Villaz-St-Pierre, Switzerland) equipped with a Bluepoint 4 UV lamp (specifications given in 'Safranin-O staining'). The polymer mixture was loaded into a cartridge equilibrated at 37 °C, and extruded through a CF300H microvalve by a pneumatically driven robotic dispenser. Hydrogel filaments and hydrogel grids with strand distance ranging from 1.0 to 2.2 mm were obtained by depositing the hydrogel lines on a pre-heated (40 °C) collection plate. Each layer was UV irradiated for 3 s from a distance of 2 cm. 3D porous constructs (height = 2 mm) were generated by dispensing horizontal and vertical filaments using a strand distance of 1.5 or 1.3 mm. Samples were UV irradiated in a layer-by-layer fashion (3 s/layer from 2 cm) with additional 15 s (from 2 cm) after the printing was completed. 3D printed hydrogels were visualized and photographed using a light microscope connected to a digital camera (specifications given in 'Safranin-O staining'). Detailed settings used during the 3D printing procedure are reported in Table S1.

3. Results and discussion

3.1. Synthesis and characterization of polymers

The thermosensitive polymer $M_{10}P_{10}$ was characterized by a number average molecular weight (M_n) of 35.6 kDa (according to GPC) and 40.3 (according to ^{1}H NMR), a DM of 10.7% and a cloud point (CP) of 17 °C. Characteristics of M_0P_{10} and $M_{10}P_{10}$ were in line with previously reported findings [20] and are summarized in Table 4. GPC analysis carried out on the polysaccharides showed M_n values of 96.1 and 90.8 kDa for HA and HAMA, respectively. The similarity in M_n and PDI of HA and HAMA (chromatograms reported in Fig. S1) confirmed that no premature cross-linking or chain scission occurred during the reaction. HAMA was characterized with a DM of 22% as calculated using its ^{1}H NMR spectrum (Eq. (2)), and the same value of 22% was found by HPLC analysis.

3.2. Phase behavior of aqueous systems of $M_{10}P_{10}$ and HAMA

Phase separation of aqueous polymer mixtures composed of different concentrations of $M_{10}P_{10}$ and HAMA was studied using CLSM and HAMA-selective staining, *i.e.* safranin-O, combined with ^{1}H NMR analysis. Fig. 1 shows confocal images of polymer mixtures containing $M_{10}P_{10}$ with a concentration of 22%, and HAMA with a concentration ranging from 0 to 2%, after 1 h of incubation at 37 °C. In samples

Table 4
Characteristics of polymers before and after methacrylation.

Polymer	M_n (kDa)	PDI (–)	DM (%)	CP (°C)
M_0P_{10}	37.3[a]	2.1[a]	0[b]	35[c]
	42.6[b]			
$M_{10}P_{10}$	35.6[a]	2.2[a]	10.7[b]	17[c]
	40.3[b]			
HA	96.1[d]	1.5[d]	0[b]	n.a.
	120.0[e]			
HAMA	90.8[d]	1.6[d]	22[b]	n.a.
			22[f]	

n.a.: not applicable.

[a] Determined by GPC, using DMF containing LiCl (10 mM) as eluent and PEG with narrow molecular weight (MW) distributions as standards.

[b] Determined by ^{1}H NMR.

[c] Determined by UV–VIS spectrophotometry and defined as the onset of the increasing light scattering during a temperature ramp measurement (4–50 °C, 1 °C/min, 650 nm).

[d] Determined by GPC, using tris(hydroxymethyl)aminomethane buffer 0.1 M (pH 7.5) as eluent and dextrans with narrow MW distributions as standards.

[e] Average MW determined by the supplier using multi-angle light scattering size exclusion chromatography.
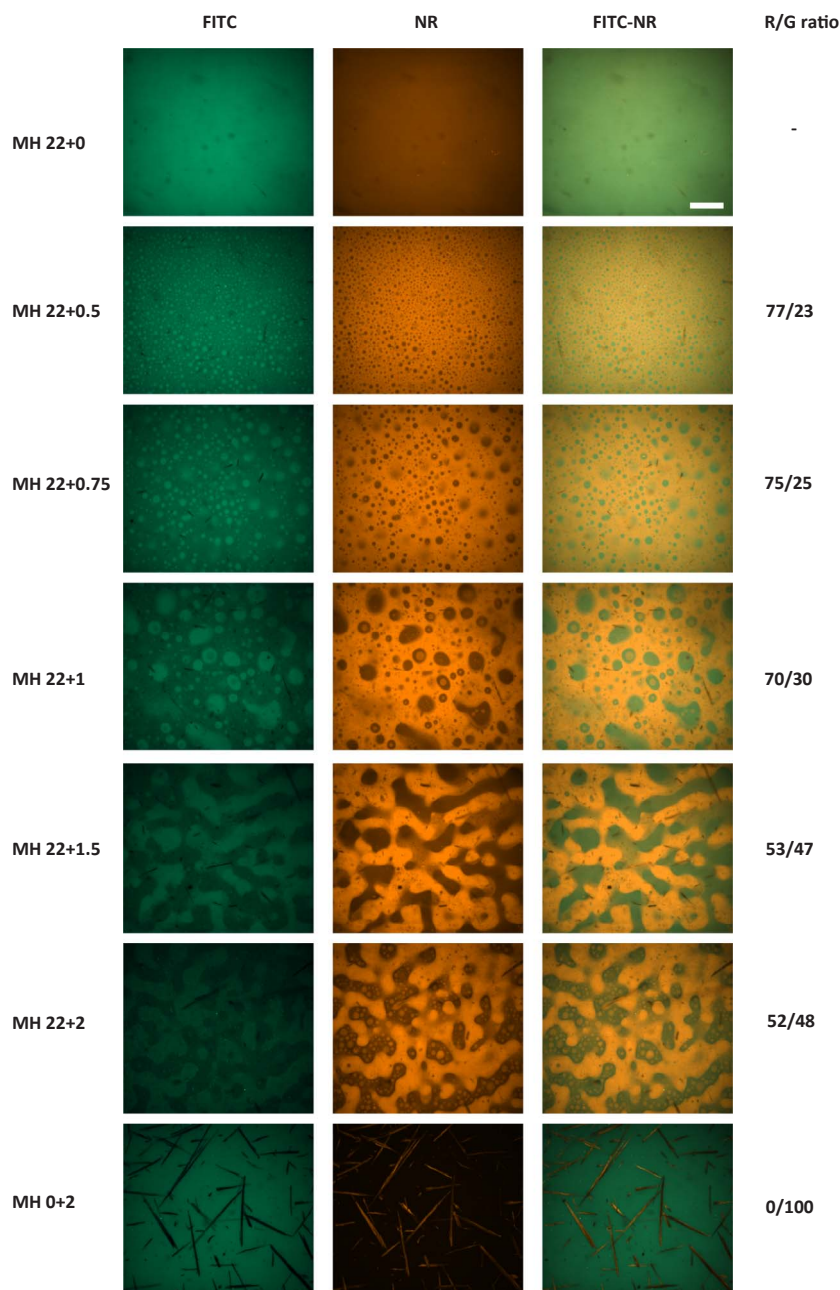
[f] Determined by HPLC.

Fig. 1. Confocal images for different MH compositions after 1 h incubation at 37 °C. FITC-BSA is visualized in green (first and third column) and NR is visualized in red (second and third column). Scale bar represents 50 μm.

containing only $M_{10}P_{10}$, a homogenous distribution of both dyes, *i.e.* FITC-BSA and NR was observed indicating that no phase separation in this system occurred on the scale of the applied magnification. Nevertheless, it needs to be mentioned that (micro-)phase separation in aqueous systems of PEG/pHPMAlac triblock copolymers can occur [21,33]. In general, ABA-like triblock copolymers with a hydrophilic mid-block and two more hydrophobic outer blocks tend to self-assemble in flower-like micelles. Moreover, by increasing the polymer concentration, bridges between adjacent micelles are formed, generating a transient physical network. In this context, phase separation can be observed between regions with high content of interconnected micelles (more dense, polymer-rich domains) and regions mostly containing isolated micelles and single polymeric chains (less dense, water-rich domains) [34]. Intuitively, this phase behavior is affected by the hydrophilic/hydrophobic balance of the polymer, which is determined by its structural characteristics (*e.g.* block length and composition) [32,52] as well as by the temperature particularly for thermosensitive systems. Therefore, the fact that we did not visualize phase separation for $M_{10}P_{10}$ mixtures in this study may be explained by the specific molecular architecture of the polymer (PEG and outer blocks length, mono/dilactate ratio in the outer blocks and DM) as well as by the applied magnification.

In samples containing only HAMA, FITC-BSA was fully and homogenously distributed, whereas NR was visible as undissolved small needles. On the other hand, for all samples containing $M_{10}P_{10}$ and HAMA a clear preferential distribution of the two dyes in specific regions was observed. FITC-BSA was mainly localized in internal domains whereas NR was dissolved in the surrounding external phase. Although a partial and consistent co-localization of the FITC-BSA in the two phases was visible using the FITC-channel (green) [21], a clear phase separation was detected using the NR-channel (red) and overlapping both channels (Fig. 1). Considering the hydrophilic character of FITC-BSA and the hydrophobic nature of NR, phase separation in $M_{10}P_{10}$/HAMA mixtures is characterized by hydrophilic internal regions, dispersed in a more hydrophobic continuous phase. The confocal images and the R/G ratios calculated for each mixture clearly show that the extent of phase separation is dependent on HAMA concentration. In general, with increasing HAMA content the internal domains became larger and more irregularly shaped, and they seemed even interconnected in MH 22 + 1.5 and MH 22 + 2. This suggests that HAMA is predominantly present in the hydrophilic dispersed phase, as also expected considering its high hydrophilicity. Interestingly, the percentage areas measured for the hydrophilic (green) regions in all the mixtures tested are much higher than the expected values based on HAMA and $M_{10}P_{10}$ solid contents. This discrepancy is likely due to the presence of also $M_{10}P_{10}$ in those domains, and more importantly, it can be explained by a dehydration process of the hydrophobic regions and consequent increase of the volume fraction of the hydrophilic phase, as it was also reported for mixtures composed of PEG and methacrylated dextran [26]. It should be noted that similar experiments carried out on UV cross-linked hydrogels revealed a similar phase separation profile (data not shown).

Mixtures containing 0.5% of HAMA and increasing concentrations of $M_{10}P_{10}$, i.e. 24 and 26% showed less extensive phase separation when compared with mixtures containing the same concentration of HAMA and 22% of $M_{10}P_{10}$ (Fig. S2). Similarly, MH 26 + 1.5 (Fig. S2) presented less phase separation in comparison to MH 22 + 1.5 (Fig. 1). Thus, the extent of phase separation decreases with increasing $M_{10}P_{10}$ content.

To investigate the kinetics of the phase separation of $M_{10}P_{10}$/HAMA mixtures, samples were analyzed by confocal microscopy at several time points within the first hour of incubation at 37 °C (Fig. S3), and after 2 h, 3 h, 8 h and 25 h of incubation at 37 °C (Fig. S4). Fig. S3 shows that for all samples containing $M_{10}P_{10}$ or $M_{10}P_{10}$ and HAMA, the intensity of the red color increased over time, likely due to the more efficient dissolution of NR after longer incubation times. Importantly, in all $M_{10}P_{10}$/HAMA blends the shape and the distribution of the internal domains did not change over time, therefore the mixtures were all stable during the first hour of incubation. For incubation times longer than 1 h, mixtures containing low HAMA concentrations, i.e. 0.5 and 0.75% were still stable over a screening period of 25 h (Fig. S4). On the contrary, confocal images of formulations with higher HA content (MH 22 + 1, MH 22 + 1.5 and MH 22 + 2) suggest that the stability over 25 h is progressively lost with gradually increasing HAMA concentration.

To verify the localization of HAMA in the phase separated gels, safranin-O assay was performed for hydrogels containing $M_{10}P_{10}$ and increasing amounts of HAMA. UV cross-linked hydrogels were used to fix the 3D polymer network for analysis, because the reversible gelation of uncross-linked samples was not compatible with several steps of this staining procedure. Fig. 2 clearly shows red-stained internal domains and an overall phase separation, which increases with increasing HAMA concentration. In MH 22 + 2 small HAMA-poor (hydrophobic) regions are present throughout HAMA-rich (hydrophilic) domains. Taken altogether, these findings are in line with the confocal images discussed above and confirmed that HAMA was exclusively present in the (more hydrophilic) dispersed phase.

To study the composition of each phase quantitatively, ^{1}H NMR analysis was used. After 1.5 h of centrifugation, polymer mixture MH 22 + 2 showed a clear macro-phase separation. ^{1}H NMR spectra of each fraction in comparison to $M_{10}P_{10}$ and HAMA spectra are shown in Fig. 3. In the spectrum of the top layer, the presence of the signal at chemical shift 3.7 representative of the CH_2 PEG protons of $M_{10}P_{10}$ together with the signal at 2.1, representative of the CH_3 protons of HAMA showed that the top layer contained both $M_{10}P_{10}$ and HAMA, with a prevalence of HAMA (HAMA/$M_{10}P_{10}$ weight ratio ~12.5/1). In line with the results obtained from the
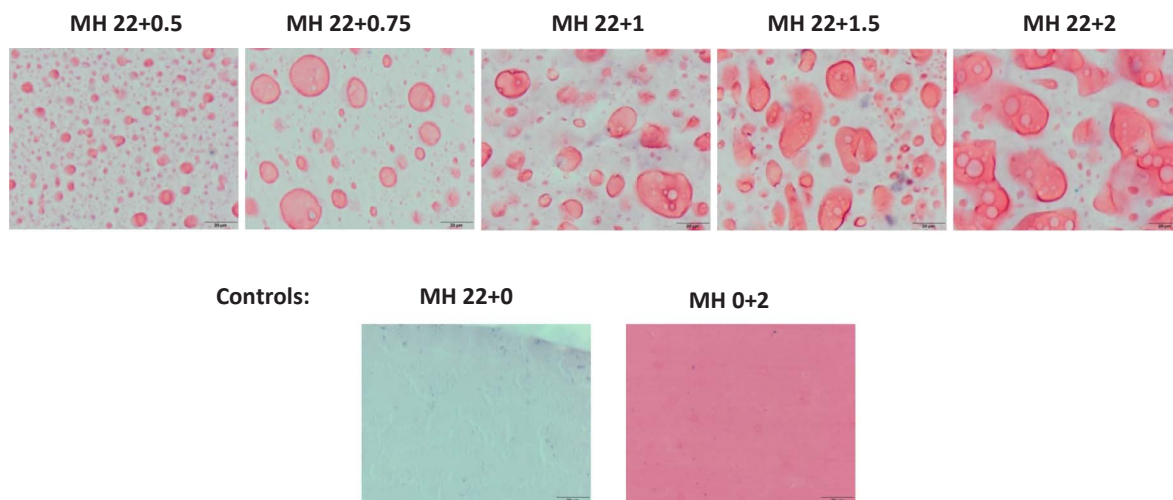

Fig. 2. Safranin-O staining for different MH compositions. HAMA is stained in red. Scale bar represents 20 μm.
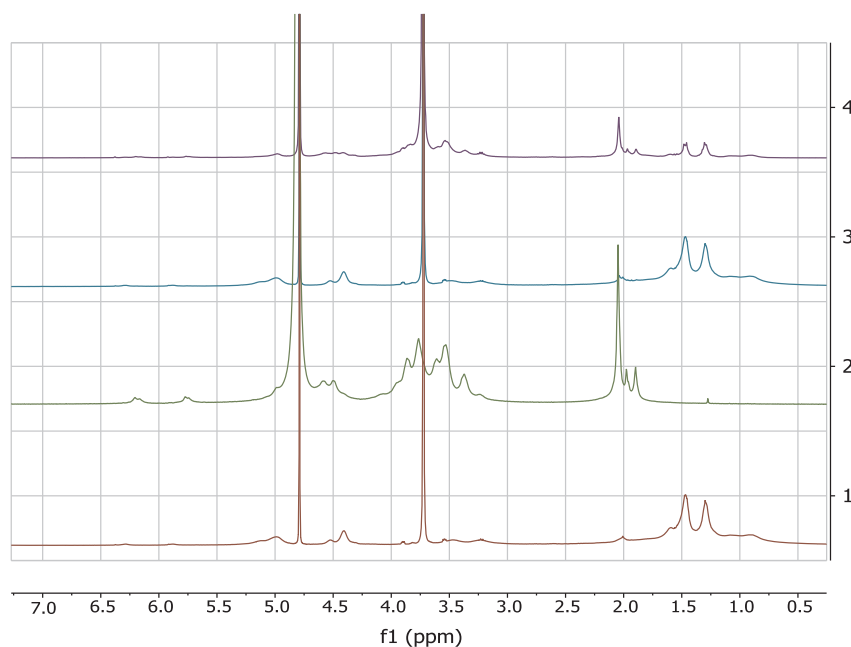
Fig. 3. ^{1}H NMR spectra of $M_{10}P_{10}$ (spectrum 1, red), HAMA (spectrum 2, green), bottom layer (spectrum 3, blue), and top layer (spectrum 4, purple). Chemical shifts were referred to the solvent (D$_2$O) residual peak of 4.79 ppm. (For interpretation of the references to colour in this figure legend, the reader is referred to the web version of this article.)

safranin-O staining, in the NMR spectrum of the bottom layer no HAMA was detected, and only the typical signals related to $M_{10}P_{10}$ were observed.

In summary, micro-scale ATPS occurs in $M_{10}P_{10}$/HAMA hydrogel mixtures. Results showed that the dispersed phase is more hydrophilic and is mainly composed of HAMA, whereas the external phase is more hydrophobic and entirely composed of $M_{10}P_{10}$. Moreover, the extent of phase separation increases with increasing HAMA content. Finally, systems with a low content of HAMA allow the formation of mixtures stable during a period of at least 25 h, whereas when the content of HAMA exceeds 1% the systems undergo a more dynamic phase separation, which increases over time.

3.3. Rheological properties

Rheological properties in oscillation and flow mode were studied in $M_{10}P_{10}$/HAMA mixtures as function of the two polymers' concentration. Fig. 4a shows the storage modulus (G′) for polymeric mixtures containing $M_{10}P_{10}$ (22%) and progressively higher concentrations of HAMA as a function of temperature. For all mixtures, an increase of G′ with increasing temperature was observed and a temperature at which G′ equals G″, here referred to as T_{gel} was identified. For samples only composed of $M_{10}P_{10}$, G′ at 37 °C was 137 ± 4 Pa and the T_{gel} was 38.6 °C. The thermosensitive behavior of pHPMAlac/PEG triblock copolymers has been reported in literature [20] and it is due to the self-assembly of polymeric chains driven by dehydration of the pHPMAlac outer blocks upon raising the temperature. In line with previously reported findings [23,24], the addition of relatively small amounts of polysaccharide, *i.e.* HAMA (0.5–1%) led to higher G′ values at 37 °C and lower T_{gel} (Fig. 4b). Remarkably, a further increase of HAMA up to 2% resulted in a lower G′ and a higher T_{gel}, despite of a higher total polymer concentration. A possible explanation for this phenomenon lies in the fact that phase separation occurs here to a higher extent. As described in 'Phase behavior of aqueous systems of $M_{10}P_{10}$ and HAMA', the formation of a hydrophilic dispersed phase is likely related to partial dehydration of the continuous more hydrophobic phase. This leads consequently to a relatively higher $M_{10}P_{10}$ concentration in the external phase, which in turn can be related to higher G′ values and lower T_{gel}. Apparently, this phenomenon positively contributes to the thermogelation profile of the hydrogel only when HAMA concentration is relatively low and, therefore when phase separation only leads to spherical hydrophilic domains. For HAMA contents higher than 1%, when the phase separation becomes more pronounced and the internal domains are interconnected (Fig. 1), the continuity of the external phase is lost and this likely leads to the observed lower G′ values of the hydrogel. Moreover, from a thermodynamic point of view, it is likely that the different shapes and sizes of the hydrophilic internal domains, as a consequence of the different HAMA concentration, have an impact on the system capacity to store energy and consequently on the rheological properties. More specifically, for low HAMA content the internal domains are spherical and for MH 22 + 0.75% larger spherical domains were observed (Fig. 1), which positively contribute to the energy storage capacity (and higher G′ values), due to their reduced overall contact surface area. On the other hand, when increasing HAMA concentration further, the irregular shape of the internal domains leads to an increase of the active surface of those domains, and consequently to higher energy dissipation by friction and lower G′ values.

Moreover, it was found that only for extensively phase-separated hydrogels, *e.g.* MH 22 + 2, the thermogelation was dependent
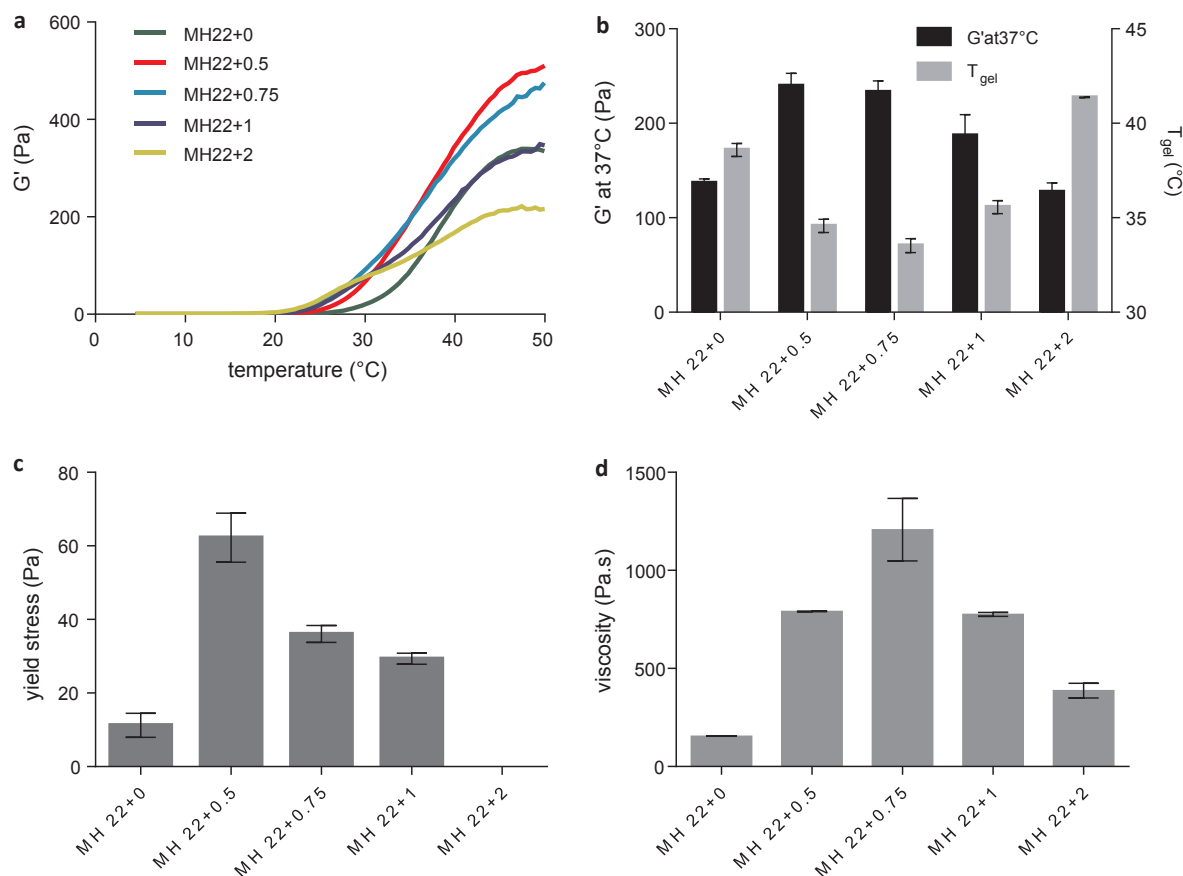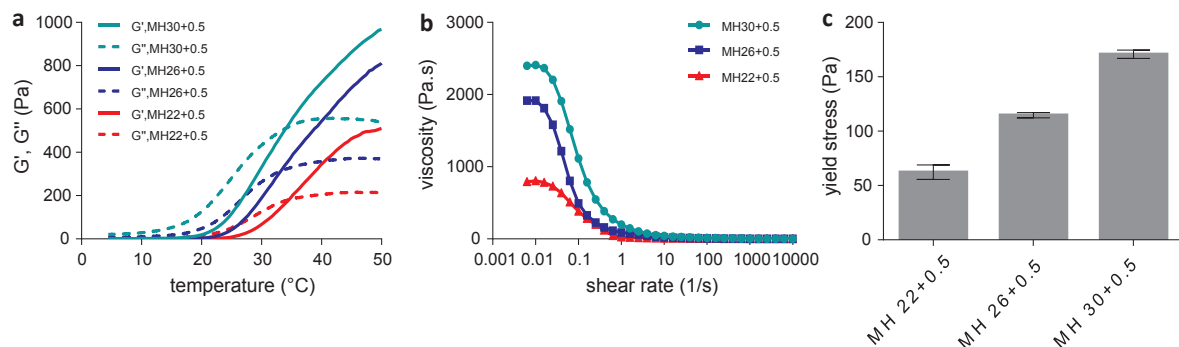
Fig. 4. Effect of HAMA concentration on hydrogel properties. G′ as function of temperature recorded during a temperature ramp (4–50 °C – 5 °C/min) using a strain of 1% and a frequency of 1 Hz for different MH formulations varying in HAMA content (a). G′ at 37 °C and T_{gel} (b). Yield stress values obtained at 37 °C during a strain sweep (0.01–100%) using a frequency of 1 Hz (c). Viscosity at 0.006 s^{-1} recorded at 37 °C during a shear rate sweep (0.006–10000 s^{-1}) (d).

on the heating rate. For these hydrogels, higher G′ values were obtained when applying a slower temperature ramp (Fig. S5a). This aspect points out the kinetics-dependent effect of phase separation and the consequent impact on rheology. On the other hand, for less phase-separated hydrogels the temperature ramp rate did not affect the thermogelation profile (Fig. S5b).

Fig. 4c reports the stress values at which G′ crosses G″, here referred to as yield stress. In line with the discussion above, a significant increase of yield stress in presence of a low amount of HAMA, *i.e.* 0.5% was observed (62.2 ± 6.7 Pa for MH 22 + 0.5) in comparison with hydrogels only composed of $M_{10}P_{10}$ (11.2 ± 3.2 Pa). When increasing HAMA content further, a progressive decrease of yield stress was observed, and remarkably, no yield stress was found for blends containing 2% of HAMA. Similar dependency on HAMA concentration was observed for viscosity at low shear and shear thinning properties of the same mixtures (Figs. 4d and S6).

The rheological study of polymeric mixtures composed of increasing amounts of $M_{10}P_{10}$ and a fixed low amount of HAMA, *i.e.*

Fig. 5. Effect of $M_{10}P_{10}$ concentration on hydrogel properties. G′ as function of temperature recorded during a temperature ramp (4–50 C – 5 °C/min) using a strain of 1% and a frequency of 1 Hz for different MH formulations varying in $M_{10}P_{10}$ content (a). Viscosity as function of shear rate recorded at 37 °C during a shear rate sweep (0.006–10000 1/s) (b). Yield stress obtained at 37 °C during a strain sweep (0.01–100%) using a frequency of 1 Hz (c).
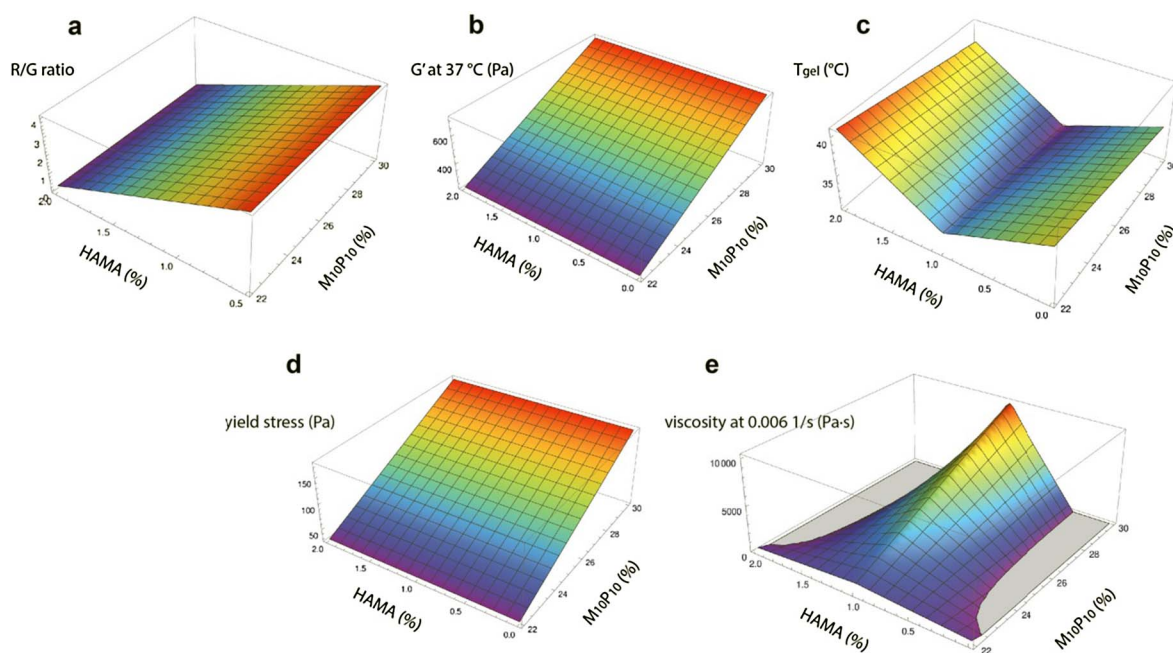
Fig. 6. Surface 3D charts based on the values predicted by the model. R/G ratio (a), G′ at 37° C (b), T_{gel} (c), yield stress (d) and viscosity at 0.006 1/s (e) as function of $M_{10}P_{10}$ and HAMA concentrations. Only positive Z values were taken into account.

0.5% showed that a higher concentration of $M_{10}P_{10}$ always contributes positively to the storage modulus, viscosity and yield stress of $M_{10}P_{10}$/HAMA mixtures (Fig. 5a–c).

Similarly to hydrogels composed of pHPMAlac/PEG triblock copolymers and a different polysaccharide, *i.e.* methacrylated chondroitin sulfate [23], hydrogels based on $M_{10}P_{10}$ and HAMA showed quick and full recovery after shear at 37 °C, which is a crucial requirement for 3D printable or injectable hydrogels (Fig. S7). Moreover, shear rate sweeps demonstrated that the viscosity at low shear rates is highly dependent on temperature. A decrease in temperature from 37 to 20 °C was responsible for significantly lower viscosity in the shear rate range of 0.006–1 s^{-1} (Fig. S8a–c). Reasonably, the full hydrogel recovery and high viscosity at elevated temperatures are linked to the thermosensitive character of $M_{10}P_{10}$.

3.4. Modeling and identification of hydrogels with selected properties

Neurofuzzylogic was employed to model the parameters, R/G ratio, G′ at 37 °C and T_{gel} recorded during oscillation temperature ramps, yield stress recorded during oscillation strain sweeps and viscosity at low shear rate (*i.e.* 0.006 s^{-1}) recorded during flow shear rate sweeps. Correlation coefficients ($74.5 < R^2 < 93.5$) together with ANOVA parameters (computed f ratio > critical f values for the degrees of freedom) for all modeled properties (Table S2) indicated that there were no statistically significant differences between experimental and predicted results. Therefore, the models can be considered having good performance and predictability. The set of rules generated for each model is reported in Table S3 and a graphical overview of the model outcome is reported in Fig. 6, where surface 3D charts are displayed. Predicted values for each *output* parameter are reported as function of HAMA and $M_{10}P_{10}$ contents. Interestingly, single effects of HAMA or/and $M_{10}P_{10}$ contribute to explain the variability of R/G ratio, G′ at 37 °C, T_{gel} and yield stress, however an interactive effect between both *inputs* determines the variation of viscosity at low shear. General trends were in line with the experimentally observed trends. Only for viscosity, despite the excellent correlation between the predicted and the experimental results (sufficiently high R^2 and significant model) some spaces were not well sampled. In those areas, the mathematical model may not fit properly.

To provide a practical example of the predictive power of the models, the inclusion criteria reported in Table 3 were used to identify a MH hydrogel composition range with selected characteristics, potentially suitable for the development of a bioink intended for nozzle-based 3D printing applications. An ideal bioink behaves as a shear thinning material able to retain its filament-like shape after extrusion, without any flow on the deposition plate (yield stress behavior). For cell-laden hydrogel printing, stability and relatively high viscosity of the material in the cartridge are desirable features to avoid cell sedimentation. On the other side, high viscosity during cell incorporation may cause handling issues [14]. Consequently, applying these requirements to MH hydrogels, sufficiently high values of yield stress, G′ at 37 °C (with low T_{gel}) and viscosity at low shear (Table 3) should ensure shape fidelity after the extrusion process. On the other side, a total polymer concentration lower than 26% (w/w) would guarantee easy handling at low temperatures and a R/G ratio higher than 75/25 would result in sufficient stability of the mixture at 37 °C in the cartridge. It has to be taken into consideration that the numerical ranges for the parameters described in the inclusion criteria were only chosen as examples and different choices can be made with respect to several aspects (*e.g.* cell-type and density, design of the aimed construct,
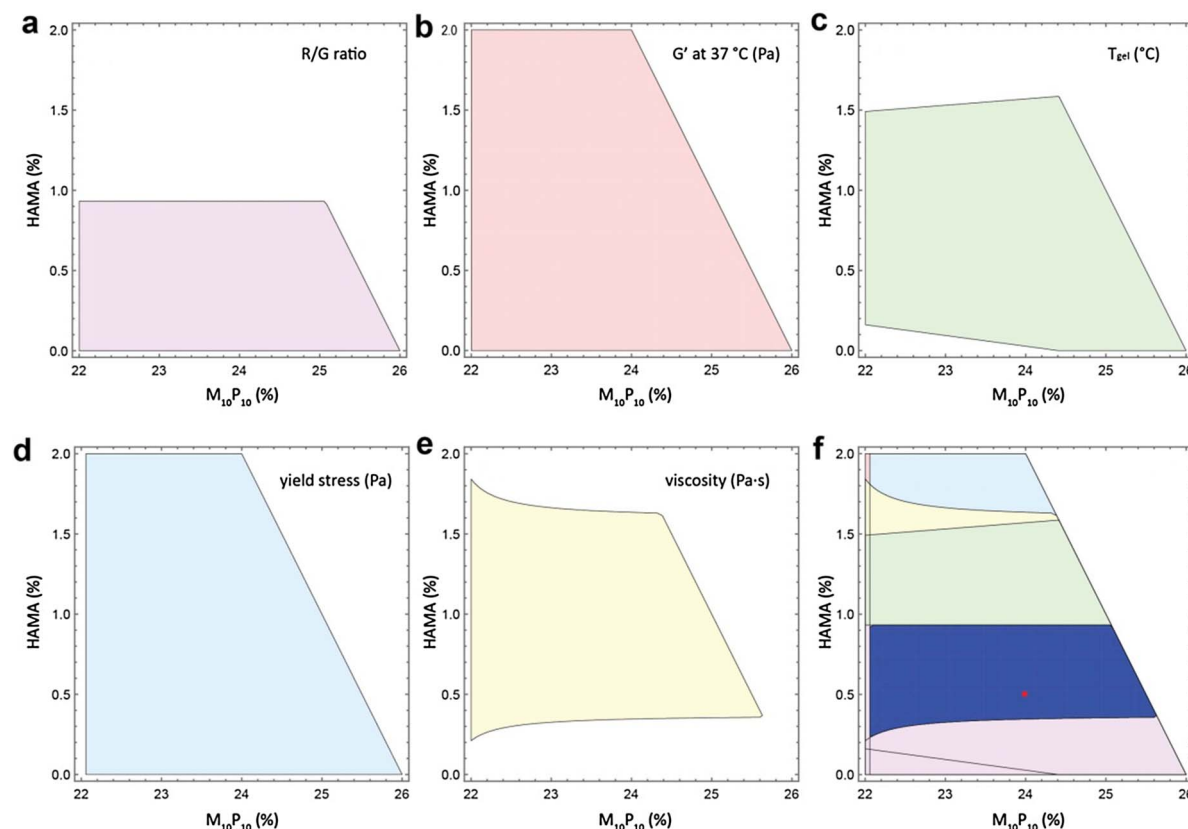
Fig. 7. 2D graphs for each *output* parameter and selected areas of interest based on the inclusion criteria reported in Table 3. Selected areas for R/G ratio (a, light purple), G′ at 37 °C (b, light pink), T_{gel} (c, light green), yield stress (d, light blue), viscosity (e, light yellow). Superimposition of selected areas for each *output* parameter; dark blue indicates the region where all the conditions are satisfied and the red dot indicates the exemplary MH composition chosen for validation of the model (f). (For interpretation of the references to colour in this figure legend, the reader is referred to the web version of this article.)

extrusion principle, etc). The superimposition of the 2D charts generated by the model for each considered *output* parameter (Fig. 7) and the implementation of the selected constraints led to the identification of a concentration range of $M_{10}P_{10}$ and HAMA (dark blue region in Fig. 7f) expected to generate hydrogels matching the selected characteristics.

MH 24 + 0.5% (red dot in Fig. 7f) was chosen as an exemplary MH composition (which was not used to generate models for the rheological properties) having $M_{10}P_{10}$ and HAMA contents in the predicted range. For MH 24 + 0.5%, G′ at 37 °C, T_{gel}, yield stress and viscosity at 0.006 1/s were found to be 372 ± 12 Pa (*vs* 349 ± 80 Pa of predicted value), 33.3 ± 0.0 °C (*vs* 34.8 ± 1.1 °C of predicted value), 117 ± 14 Pa (*vs* 66 ± 15 Pa of predicted value) and 1445 ± 36 Pa·s (*vs* 1182 ± 148 Pa·s of predicted value), respectively. In fact, these values were within the selected ranges and sufficiently close to the predicted values. Moreover, the 3D printing of MH 24 + 0.5% resulted in the generation of shape-stable filaments and grids with strand distance ranging from 1.0 to 2.2 mm (Fig. 8a and b). Furthermore, 2 mm high and porous constructs with variable strand distance (1.3 and 1.5 mm) were successfully printed (Fig. 8c–f).

All printed constructs were shape-stable, before and after swelling in PBS, as they were handled by the use of a spatula without damage. Taken all together, we developed a valid model for the prediction of the phase behavior and rheological properties of MH hydrogels and showed its applicability for the identification of hydrogel compositions with pre-designed, desirable profiles.

4. Conclusions

Hydrogels composed of $M_{10}P_{10}$ and HAMA showed phase separation within the studied concentration range. The co-existence of a more hydrophilic, HAMA-richer dispersed phase together with a more hydrophobic and partially dehydrated $M_{10}P_{10}$-based continuous phase was found to be a crucial structural characteristic, that directly affected the rheological behavior of these hydrogels. Limited phase separation, corresponding to low concentrations of HAMA was responsible for higher values of storage modulus, yield stress and viscosity, which is potentially beneficial for nozzle-based 3D printing applications of these materials. Partial dehydration of the continuous phase resulted in a higher concentration of $M_{10}P_{10}$ in this phase, which is likely responsible for the observed changes in rheological properties. On the other hand, extensive phase separation upon addition of high concentrations of HAMA negatively affected the rheological profile, because of loss of continuity in the external phase. Considering the complex dependency of phase behavior and
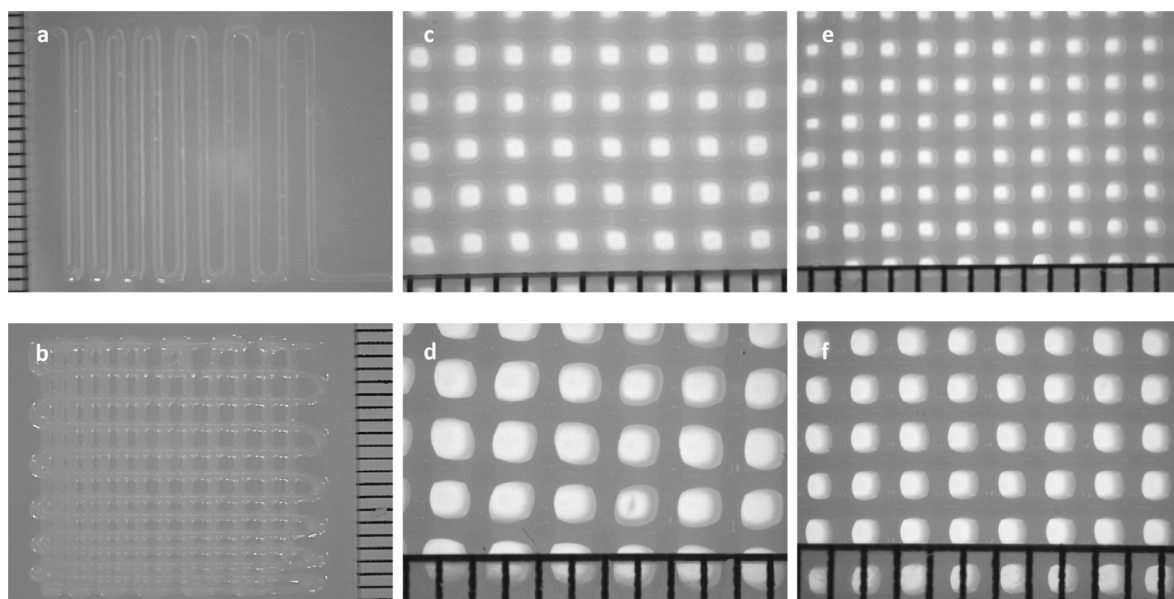
Fig. 8. 3D printing of an exemplary MH hydrogel composition with selected properties as predicted by the model, *i.e.* MH 24 + 0.5. Hydrogel filament with strand distance ranging from 1 mm to 2.2 mm (a). Hydrogel grid with strand distance ranging from 1 mm to 2.2 mm (b). 3D construct (20 layers, height = 2 mm) with strand distance 1.5 mm (c and d). 3D construct (20 layers, height = 2 mm) with strand distance 1.3 mm (e and f). Line between two consecutive marks on the ruler indicates 1 mm.

rheology from the two polymer concentrations, a computational model was generated to predict *a priori* hydrogel compositions displaying desirable and selected characteristics. In general, the ANNs-based approach can be potentially applied to any kind of hydrogel material and it can be a useful tool especially for developing hydrogels of complex composition.

Acknowledgments

Appendix A. Supplementary material

Supplementary data associated with this article can be found, in the online version, at http://dx.doi.org/10.1016/j.eurpolymj. 2017.04.029.

References

[1] S. Ahadian, R.B. Sadeghian, S. Salehi, S. Ostrovidov, H. Bae, M. Ramalingam, A. Khademhosseini, Bioconjugated hydrogels for tissue engineering and regenerative medicine, Bioconjug. Chem. 26 (2015) 1984–2001, http://dx.doi.org/10.1021/acs.bioconjchem.5b00360.
[2] R. Censi, P. Di Martino, T. Vermonden, W.E. Hennink, Hydrogels for protein delivery in tissue engineering, J. Control. Release 161 (2012) 680–692, http://dx.doi.org/10.1016/j.jconrel.2012.03.002.
[3] T. Vermonden, R. Censi, W.E. Hennink, Hydrogels for protein delivery, Chem. Rev. 112 (2012) 2853–2888, http://dx.doi.org/10.1021/cr200157d.
[4] M.W. Tibbitt, J.E. Dahlman, R. Langer, Emerging frontiers in drug delivery, J. Am. Chem. Soc. 138 (2016) 704–717, http://dx.doi.org/10.1021/jacs.5b09974.
[5] E. Caló, V.V. Khutoryanskiy, Biomedical applications of hydrogels: a review of patents and commercial products, Eur. Polym. J. 65 (2015) 252–267, http://dx.doi.org/10.1016/j.eurpolymj.2014.11.024.
[6] N. Hammer, F.P. Brandl, S. Kirchhof, V. Messmann, A.M. Goepferich, Protein compatibility of selected cross-linking reactions for hydrogels, Macromol. Biosci. 15 (2015) 405–413, http://dx.doi.org/10.1002/mabi.201400379.
[7] M.C. Koetting, J.T. Peters, S.D. Steichen, N.A. Peppas, Stimulus-responsive hydrogels: theory, modern advances, and applications, Mater. Sci. Eng. R Rep. 93 (2015) 1–49, http://dx.doi.org/10.1016/j.mser.2015.04.001.
[8] S.J. Buwalda, K.W.M. Boere, P.J. Dijkstra, J. Feijen, T. Vermonden, W.E. Hennink, Hydrogels in a historical perspective: from simple networks to smart materials, J. Control. Release 190 (2014) 254–273, http://dx.doi.org/10.1016/j.jconrel.2014.03.052.
[9] N. Annabi, A. Tamayol, J.A. Uquillas, M. Akbari, L.E. Bertassoni, C. Cha, G. Camci-Unal, M.R. Dokmeci, N.A. Peppas, A. Khademhosseini, 25th anniversary article: rational design and applications of hydrogels in regenerative medicine, Adv. Mater. 26 (2014) 85–124, http://dx.doi.org/10.1002/adma.201303233.
[10] D.W. Hutmacher, Scaffolds in tissue engineering bone and cartilage, Biomaterials 21 (2000) 2529–2543, http://dx.doi.org/10.1016/S0142-9612(00)00121-6.
[11] C. Madeira, A. Santhagunam, J.B. Salgueiro, J.M.S. Cabral, Advanced cell therapies for articular cartilage regeneration, Trends Biotechnol. 33 (2015) 35–42, http://dx.doi.org/10.1016/j.tibtech.2014.11.003.
[12] J.A. Hunt, R. Chen, T. van Veen, N. Bryan, Hydrogels for tissue engineering and regenerative medicine, J. Mater. Chem. B 2 (2014) 5319–5338, http://dx.doi.org/10.1039/C4TB00775A.
[13] D.M. Kirchmajer, R. Gorkin III, M. in het Panhuis, An overview of the suitability of hydrogel-forming polymers for extrusion-based 3D-printing, J. Mater. Chem.

B. 3 (2015) 4105–4117. http://dx.doi.org/10.1039/C5TB00393H.

[14] T. Jungst, W. Smolan, K. Schacht, T. Scheibel, J. Groll, Strategies and molecular design criteria for 3D printable hydrogels, Chem. Rev. 116 (2016) 1496–1539, http://dx.doi.org/10.1021/acs.chemrev.5b00303.

[15] V.K. Lee, G. Dai, Printing of three-dimensional tissue analogs for regenerative medicine, Ann. Biomed. Eng. (2016), http://dx.doi.org/10.1007/s10439-016-1613-7.

[16] R.R. Jose, M.J. Rodriguez, T.A. Dixon, F. Omenetto, D.L. Kaplan, Evolution of bioinks and additive manufacturing technologies for 3D bioprinting, ACS Biomater. Sci. Eng. 2 (2016) 1662–1678, http://dx.doi.org/10.1021/acsbiomaterials.6b00088.

[17] J. Malda, J. Visser, F.P. Melchels, T. Jüngst, W.E. Hennink, W.J.A. Dhert, J. Groll, D.W. Hutmacher, 25th anniversary article: engineering hydrogels for biofabrication, Adv. Mater. 25 (2013) 5011–5028, http://dx.doi.org/10.1002/adma.201302042.

[18] F.P.W. Melchels, J. Feijen, D.W. Grijpma, A review on stereolithography and its applications in biomedical engineering, Biomaterials 31 (2010) 6121–6130, http://dx.doi.org/10.1016/j.biomaterials.2010.04.050.

[19] F.P.W. Melchels, M.A.N. Domingos, T.J. Klein, J. Malda, P.J. Bartolo, D.W. Hutmacher, Additive manufacturing of tissues and organs, Prog. Polym. Sci. 37 (2012) 1079–1104, http://dx.doi.org/10.1016/j.progpolymsci.2011.11.007.

[20] T. Vermonden, N.E. Fedorovich, D. van Geemen, J. Alblas, C.F. van Nostrum, W.J.A. Dhert, W.E. Hennink, Photopolymerized thermosensitive hydrogels: synthesis, degradation, and cytocompatibility, Biomacromol 9 (2008) 919–926, http://dx.doi.org/10.1021/bm7013075.

[21] R. Censi, T. Vermonden, H. Deschout, K. Braeckmans, P. di Martino, S.C. De Smedt, C.F. van Nostrum, W.E. Hennink, Photopolymerized thermosensitive poly (HPMAlactate)-PEG-based hydrogels: effect of network design on mechanical properties, degradation, and release behavior, Biomacromol 11 (2010) 2143–2151, http://dx.doi.org/10.1021/bm100514p.

[22] R. Censi, W. Schuurman, J. Malda, G. di Dato, P.E. Burgisser, W.J.A. Dhert, C.F. van Nostrum, P. di Martino, T. Vermonden, W.E. Hennink, A printable photopolymerizable thermosensitive p(HPMAm-lactate)-PEG hydrogel for tissue engineering, Adv. Funct. Mater. 21 (2011) 1833–1842, http://dx.doi.org/10.1002/adfm.201002428.

[23] A. Abbadessa, M.M. Blokzijl, V.H.M. Mouser, P. Marica, J. Malda, W.E. Hennink, T. Vermonden, A thermo-responsive and photo-polymerizable chondroitin sulfate-based hydrogel for 3D printing applications, Carbohyd. Polym. 149 (2016) 163–174, http://dx.doi.org/10.1016/j.carbpol.2016.04.080.

[24] A. Abbadessa, V.H.M. Mouser, M.M. Blokzijl, D. Gawlitta, W.J.A. Dhert, W.E. Hennink, J. Malda, T. Vermonden, A synthetic thermosensitive hydrogel for cartilage bioprinting and its biofunctionalization with polysaccharides, Biomacromolecules 17 (2016) 2137–2147, http://dx.doi.org/10.1021/acs.biomac.6b00366.

[25] P.-Å. Albertsson, Particle fractionation in liquid two-phase systems. The composition of some phase systems and the behaviour of some model particles in them. Application to the isolation of cell walls from microorganisms, Biochem. Biophys. Acta. 27 (1958) 378–395, http://dx.doi.org/10.1016/0006-3002(58)90345-7.

[26] R.J.H. Stenekes, O. Franssen, E.M.G. van Bommel, D.J.A. Crommelin, W.E. Hennink, The preparation of dextran microspheres in an all-aqueous system: effect of the formulation parameters on particle characteristics, Pharm. Res. 15 (1998) 557–561, http://dx.doi.org/10.1023/A:1011925709873.

[27] O. Franssen, W.E. Hennink, A novel preparation method for polymeric microparticles without the use of organic solvents, Int. J. Pharm. 168 (1998) 1–7, http://dx.doi.org/10.1016/S0378-5173(98)00071-4.

[28] P.-Å. Albertsson, Partition of cell particles and macromolecules in polymer two-phase systems, Arch. Biochem. Biophys. (1970) 309–341, http://dx.doi.org/10.1016/S0065-3233(08)60244-2.

[29] R. Hatti-Kaul, Aqueous two-phase systems: a general overview, Mol. Biotechnol. 19 (2001) 269–278, http://dx.doi.org/10.1385/MB:19:3:269.

[30] H.-O. Johansson, F.M. Magaldi, E. Feitosa, A. Pessoa, Protein partitioning in poly(ethylene glycol)/sodium polyacrylate aqueous two-phase systems, J. Chromatogr. A 1178 (2008) 145–153, http://dx.doi.org/10.1016/j.chroma.2007.11.071.

[31] P.A. Levett, F.P.W. Melchels, K. Schrobback, D.W. Hutmacher, J. Malda, T.J. Klein, A biomimetic extracellular matrix for cartilage tissue engineering centered on photocurable gelatin, hyaluronic acid and chondroitin sulfate, Acta Biomater. 10 (2014) 214–223, http://dx.doi.org/10.1016/j.actbio.2013.10.005.

[32] J. François, E. Beaudoin, O. Borisov, Association of hydrophobically end-capped poly(ethylene oxide). 2. Phase diagrams, Langmuir 19 (2003) 10011–10018, http://dx.doi.org/10.1021/la0208833.

[33] T. Vermonden, S.S. Jena, D. Barriet, R. Censi, J. van der Gucht, W.E. Hennink, R.A. Siegel, Macromolecular diffusion in self-assembling biodegradable thermosensitive hydrogels, Macromolecules 43 (2010) 782–789, http://dx.doi.org/10.1021/ma902186e.

[34] A.N. Semenov, J.-F. Joanny, A.R. Khokhlov, Associating polymers: equilibrium and linear viscoelasticity, Macromolecules 28 (1995) 1066–1075, http://dx.doi.org/10.1021/ma00108a038.

[35] M.H.M. Oudshoorn, R. Rissmann, J.A. Bouwstra, W.E. Hennink, Synthesis and characterization of hyperbranched polyglycerol hydrogels, Biomaterials 27 (2006) 5471–5479, http://dx.doi.org/10.1016/j.biomaterials.2006.06.030.

[36] A.S. Achanta, J.G. Kowalski, C.T. Rhodes, Artificial neural networks: implications for pharmaceutical sciences, Drug Dev. Ind. Pharm. 21 (1995) 119–155, http://dx.doi.org/10.3109/03639049509048099.

[37] F. Kazazi-Hyseni, M. Landin, A. Lathuile, G.J. Veldhuis, S. Rahimian, W.E. Hennink, R.J. Kok, C.F. van Nostrum, Computer modeling assisted design of monodisperse PLGA microspheres with controlled porosity affords zero order release of an encapsulated macromolecule for 3 months, Pharm. Res. (2014) 2844–2856, http://dx.doi.org/10.1007/s11095-014-1381-8.

[38] D. Nauck, R. Kruse, A neuro-fuzzy method to learn fuzzy classification rules from data, Fuzzy Sets Syst. 89 (1997) 277–288, http://dx.doi.org/10.1016/S0165-0114(97)00009-2.

[39] M. Landin, R.C. Rowe, Artificial neural networks technology to model, understand, and optimize drug formulations, in: Formul. Tools Pharm. Dev., J. Aguilar, Elsevier, 2013, pp. 7–37. http://dx.doi.org/10.1533/9781908818508.7.

[40] C.J. Rijcken, C.J. Snel, R.M. Schiffelers, C.F. van Nostrum, W.E. Hennink, Hydrolysable core-crosslinked thermosensitive polymeric micelles: synthesis, characterisation and in vivo studies, Biomaterials 28 (2007) 5581–5593, http://dx.doi.org/10.1016/j.biomaterials.2007.08.047.

[41] E. Hachet, H. Van Den Berghe, E. Bayma, M.R. Block, R. Auzély-Velty, Design of biomimetic cell-interactive substrates using hyaluronic acid hydrogels with tunable mechanical properties, Biomacromolecules 13 (2012) 1818–1827, http://dx.doi.org/10.1021/bm300324m.

[42] R.J.H. Stenekes, W.E. Hennink, Polymerization kinetics of dextran-bound methacrylate in an aqueous two phase system, Polymer 41 (2000) 5563–5569, http://dx.doi.org/10.1016/S0032-3861(99)00814-9.

[43] T. Vermonden, N.A.M. Besseling, M.J. van Steenbergen, W.E. Hennink, Rheological studies of thermosensitive triblock copolymer hydrogels, Langmuir 22 (2006) 10180–10184, http://dx.doi.org/10.1021/la062224m.

[44] O.F.W. Gardner, G. Musumeci, A.J. Neumann, D. Eglin, C.W. Archer, M. Alini, M.J. Stoddart, Asymmetrical seeding of MSCs into fibrin-poly(ester-urethane) scaffolds and its effect on mechanically induced chondrogenesis, J. Tissue Eng. Regen. Med. (2016), http://dx.doi.org/10.1002/term.2194.

[45] C.M. Shih, J.T. Chien, The microscopic pictures of degenerative intervertebral disc of different diseases with additional safranin-O stain, J. Clin. Exp. Pathol. 6 (2015) 1–5, http://dx.doi.org/10.4172/2161-0681.1000265.

[46] M. Barandun, L.D. Iselin, F. Santini, M. Pansini, C. Scotti, D. Baumhoer, O. Bieri, U. Studler, D. Wirz, M. Haug, M. Jakob, D.J. Schaefer, I. Martin, A. Barbero, Generation and characterization of osteochondral grafts with human nasal chondrocytes, J. Orthop. Res. 33 (2015) 1111–1119, http://dx.doi.org/10.1002/jor.22865.

[47] M. Younesi, V.M. Goldberg, O. Akkus, A micro-architecturally biomimetic collagen template for mesenchymal condensation based cartilage regeneration, Acta Biomater. 30 (2016) 212–221, http://dx.doi.org/10.1016/j.actbio.2015.11.024.

[48] H. Hsu, T. Uemura, I. Yamaguchi, T. Ikoma, J. Tanaka, Chondrogenic differentiation of human mesenchymal stem cells on fish scale collagen, J. Biosci. Bioeng. 122 (2016) 219–225, http://dx.doi.org/10.1016/j.jbiosc.2016.01.001.

[49] H.-J. Prins, A.K. Braat, D. Gawlitta, W.J.A. Dhert, D.A. Egan, E. Tijssen-Slump, H. Yuan, P.J. Coffer, H. Rozemuller, A.C. Martens, In vitro induction of alkaline phosphatase levels predicts in vivo bone forming capacity of human bone marrow stromal cells, Stem Cell Res. 12 (2014) 428–440, http://dx.doi.org/10.1016/j.scr.2013.12.001.

[50] D. Kokkinis, M. Schaffner, A.R. Studart, Multimaterial magnetically assisted 3D printing of composite materials, Nat. Commun. 6 (2015) 8643, http://dx.doi.org/10.1038/ncomms9643.

[51] M. Zhang, A. Vora, W. Han, R.J. Wojtecki, H. Maune, A.B.A. Le, L.E. Thompson, G.M. McClelland, F. Ribet, A.C. Engler, A. Nelson, Dual-responsive hydrogels for direct-write 3D printing, Macromolecules 48 (2015) 6482–6488, http://dx.doi.org/10.1021/acs.macromol.5b01550.

[52] J. Sprakel, N.A.M. Besseling, M.A. Cohen Stuart, F.A.M. Leermakers, Phase behavior of flowerlike micelles in a SCF cell model, Eur. Phys. J. E 25 (2008) 163–173, http://dx.doi.org/10.1140/epje/i2007-10277-1.